

Chapter 9

Patterned Photostimulation in the Brain

Francesca Anselmi, Arkarup Banerjee and Dinu F. Albeanu

Abstract Photostimulation has been instrumental in the past two decades for studying the structural synaptic plasticity and functional connectivity of neuronal circuits. With the advent of optogenetic strategies, this approach has been further expanded and used to identify the neuronal substrates of behavior via monitoring and modulating the activity of specific neuronal types *in vivo*. To date, however, photostimulation has been mainly implemented via full-field illumination and laser scanning protocols, which suffer from limited selectivity and stop short of generating asynchronous and spatially distributed neuronal firing patterns, characteristic for brain activity.

In this chapter, we discuss advances in using novel light patterning techniques which allow shaping illumination to create flexible spatiotemporal photostimulation profiles over large ensembles of neurons, as well as onto subcellular compartments. Specifically, we describe two light patterning strategies implemented through intensity and phase modulation, respectively. We illustrate the underlying physical principles, their applications to date, and the scope and limitations of each method, in an attempt to bridge the gap between the development of optical techniques and their use for neuroscience experiments.

9.1 Introduction

A central goal of systems neuroscience is to describe behaviors in terms of the neuronal circuits that control them. This is particularly challenging in the mammalian brain because behaviors are thought to rely on widely distributed neuronal representations that are technically difficult to monitor at large scales, or to

D. F. Albeanu (✉) · F. Anselmi · A. Banerjee
Cold Spring Harbor Laboratory, Cold Spring Harbor, NY 11724, USA
e-mail: albeanu@cshl.edu

A. Banerjee · D. F. Albeanu
Watson School of Biological Sciences, Cold Spring Harbor, NY 11724, USA

manipulate at cellular resolution. Understanding the function of neuronal circuits requires monitoring large populations of neurons in the intact brain, while simultaneously perturbing specific circuit elements. This is a hard problem since functional imaging and electrophysiology studies have revealed that neuronal representations of sensory-motor information in many brain regions are spatially distributed and asynchronous. In addition, the spatial and temporal scales of physiological phenomena vary widely. Depending upon the question of interest, one may need to probe neuronal activity at micrometric scale, at the network level, or across brain regions, over milliseconds to several days.

In the past two decades, due to its noninvasive nature, light has been used as a tool to monitor the structure and activity of neuronal systems [1]. The flexibility in design of functional imaging setups, together with the diversity of available chemical and genetically encoded calcium [2–4] and voltage [5–7] indicators, have allowed researchers to address a wide range of issues ranging from structural synaptic plasticity [8, 9], dendritic integration [10–14], and functional connectivity [15–18] to circuit dynamics and the neuronal substrates of behavior [19–21].

As a complement to functional imaging, photostimulation techniques can be used to probe brain circuits by specifically manipulating neuronal activity. In particular, the advent of optogenetic actuators, allowing bidirectional control of neuronal firing [22–24], has made it feasible to map functional connectivity across the brain and assess the roles of genetically identified neuronal types in network computations [25]. Furthermore, this approach has advanced our understanding of brain architecture and function by relating anatomical structures to their roles in behavior. Commonly used photostimulation techniques have the advantage of simplicity, as they rely on genetic targeting to determine the specificity of stimulation and on the use of full-field illumination (mostly through optical fibers) to deliver light into brain preparations [26, 27]. Technical accessibility has, indeed, been an important factor in ensuring the fast spread and success of optogenetic manipulations.

However, of late scientists have started investigating the potential of more sophisticated optical techniques to overcome some limitations of full-field light stimulation [28, 29]. We describe in this chapter, two innovative optical methods referred to as *light patterning techniques* that enable simultaneous stimulation of multiple neuronal targets by flexibly shaping the illumination. Patterned illumination strategies allow the generation of flexible spatial and temporal photostimulation profiles, which, in combination with multiphoton imaging of neuronal activity, electrophysiological recordings, and optogenetic manipulations, provide an ideal framework toward achieving optical control of neuronal activity.

9.1.1 Why Do We Need Light Patterning?

Until recently, targeted photostimulation and imaging of multiple neuronal structures have been almost exclusively performed by sequential scanning. In this approach, a *collimated* laser beam is either focused by an objective lens in a *diffraction-limited*

volume or sent into the sample as a pencil of parallel light and steered through the field of stimulation by galvanometric mirrors. Laser scanning photostimulation has been successfully used in conjunction with uncaging of neurotransmitters [30–35] and in optogenetic experiments that map functional connectivity in [36–38]. The major limitation of this approach lies in the need to sequentially stimulate multiple targets. Although recent techniques such as resonant scanning [39, 40] and acousto-optical deflectors (AODs) [41–44] have allowed scanning at high frequencies (hundreds of Hz to KHz), the actual number of targets that can be stimulated within a physiologically relevant time window (a few milliseconds) remains constrained by the dwell time at each site. In turn, the dwell time is determined by the specifics of the excitation process and the photochemical properties of light-sensitive compounds. In the case of optogenetic actuators (opsins), these also include activation time and single-channel conductance [45, 46]. Thus, sequential approaches become unfavorable in experiments where a large number of sites needs to be probed and when the necessary dwell time is on the order of a millisecond or longer [47]. Under these conditions, patterned illumination techniques that shape the stimulation light in order to target multiple structures simultaneously provide a valuable alternative.

9.1.2 General Principles of Light Patterning

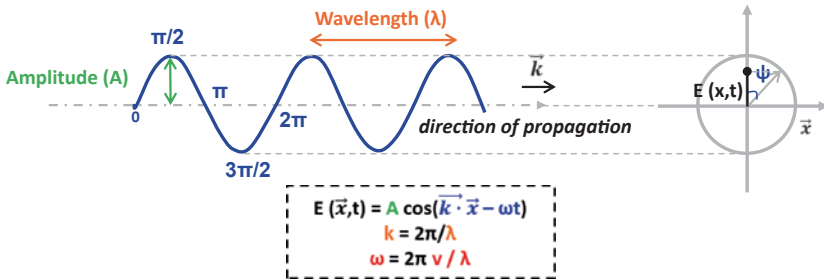
A simple example of light patterning is a configuration where the sample is illuminated by an array of *micro-LEDs* (Fig. 9.1a). The illumination light path in the microscope can be set up such that an image of the array is formed at the *focal plane* of the objective lens (Sect. 9.2.1). In this case, by switching ON and OFF any micro-LED in the array, the user can gate the illumination within corresponding regions in the sample (Fig. 9.1a). This principle of operation is general in light patterning techniques, where the illumination of the sample is shaped by an array of discrete actuators, generally referred to as spatial light modulator (SLM), placed in a remote location, but optically coupled to the focal plane of the microscope objective.

To understand the physical principles behind different types of light patterning strategies, it is convenient to introduce a formal notation, which describes light as an oscillating electromagnetic field. The light electromagnetic field, as any other propagating wave (Box 1), is a function of both space and time (imagine ripples in a pond). However, in the context of light patterning, the temporal dimension can be discarded, as if taking a snapshot at a particular moment, and light can be described as an electromagnetic field oscillating in space. Along the same lines, it is sufficient to represent light as an oscillating electric field:

$$E(\vec{r}) = A(\vec{r})e^{i\psi(\vec{r})} \quad (9.1)$$

where $A(\vec{r})$ is the maximum amplitude of the oscillation in a given location \vec{r} and $\psi(\vec{r})$ is its phase, that is the angle within the oscillation cycle (Box 1).

BOX 1: Wave Propagation



The amplitude of a wave propagating in one dimension (x) can be represented as a periodic function described in terms of sines and/or cosines. For example:

$$E(\vec{k}\vec{x}) = A \cos(\vec{k}, \vec{x}), \tag{9.14}$$

where, A is the maximum amplitude of the oscillation and \vec{k} is the wave vector of magnitude $2\pi/\lambda$, whose direction corresponds to the propagation direction. To describe a propagating wave with velocity \vec{v} , Eq. (9.14) is modified to include a constant (a) (ω , angular velocity) denoting how much the wave has travelled in a time interval, t .

$$E(\vec{x}, t) = A \cos(\vec{k} \cdot (\vec{x} - \vec{v}t)) = A \cos(\vec{k} \cdot \vec{x} - \omega t) = A \cos \psi \tag{9.15}$$

The argument of the cosine term (ψ) denotes the relative position within the oscillation cycle, also known as phase.

The above equation can be rewritten in terms of exponentials using the Euler’s formula:

$$Ae^{i\psi} = A \cos \psi + iA \sin \psi, \tag{9.16}$$

where

$$Real(Ae^{i\psi}) = A \cos \psi \tag{9.17}$$

For mathematical convenience, usually the imaginary part is also included in the equation which can be written in an exponential form:

$$E(x, t) = \cos \psi + i \sin \psi = Ae^{i\psi} \tag{9.18}$$

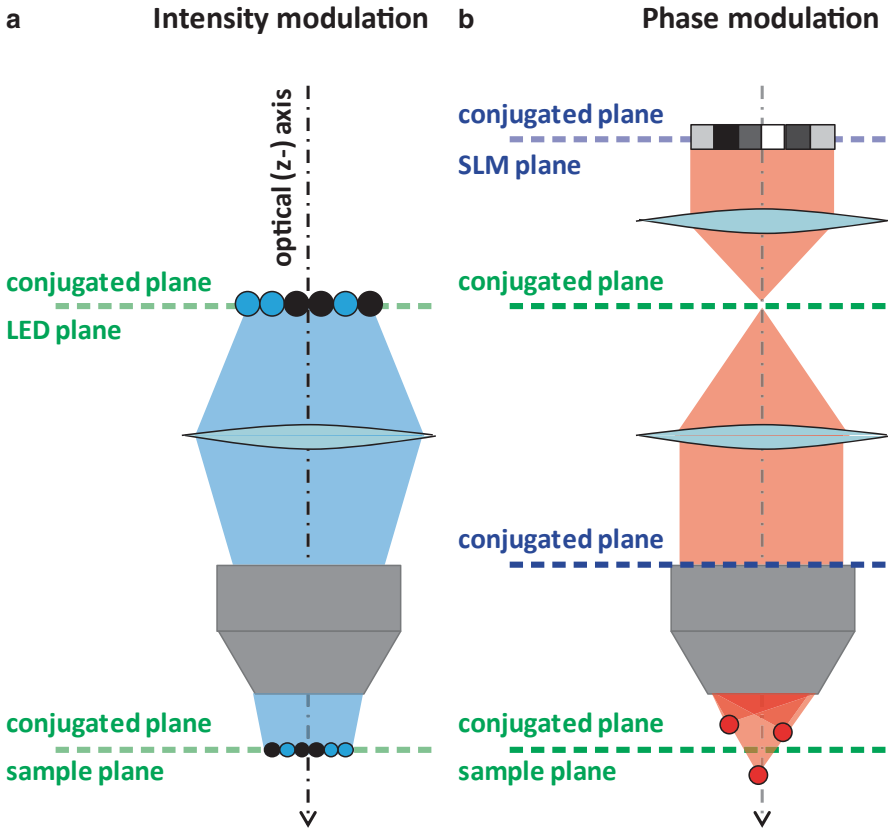


Fig. 9.1 Light patterning. Cartoon schematics illustrating the general principle of intensity (**a**) and phase (**b**) modulation. **a** Intensity modulation is obtained by placing a digital micromirror devices (DMD) or an LED array in a plane conjugated with the sample plane, such that the intensity pattern generated by the DMD/LED is imaged into the sample. **b** Phase modulation is obtained by placing an SLM in a plane conjugated with the back focal plane of the microscope objective. The phase profiles generated by the SLM are transformed by the objective lens into the desired intensity pattern at the sample

In order to perform light patterning, the amplitude of the light electric field at the sample ($E(\vec{r})$) needs to be modulated. This is implemented by modifying either the intensity ($I(\vec{r}) \propto |\vec{E}|^2$) or the phase ($\psi(\vec{r})$) of the light electric field at a remote location using an SLM. One very convenient remote location is a plane *conjugated* to the front focal plane of the microscope objective. An SLM placed at this particular location will be imaged at the sample (the front focal plane of the objective, Fig. 9.1a). If the maximum amplitude of the light electric field ($A(\vec{r})$) is modulated at the SLM plane, the same modulation will apply to all conjugated planes, one of which is the sample plane. This strategy is extensively used in “intensity-modulation” light patterning techniques, described in Sect. 9.2. However,

this is not the only option. Another possibility is to modulate the phase of the light electric field ($\psi(\vec{r})$) in order to create specific interference patterns that generate the desired light intensity pattern at the sample (Fig. 9.1b). This strategy is adopted in “phase-modulation” light patterning techniques, such as digital holography described in Sect. 9.3.

As defined above, the term SLM applies to any device used for either intensity or phase-modulation light patterning techniques. However, numerous studies in the field use it to refer specifically to phase-modulation devices, as we will also do throughout this chapter.

9.2 Light Patterning by Intensity Modulation

9.2.1 General Principle

A simple way of achieving light patterning is by using a light source composed of discrete actuators that can be individually turned ON and OFF. If such a source is imaged onto the sample (Fig. 9.1a), this results in a 2D pixelated illumination profile, which can be flexibly shaped. A common way of implementing this idea is to place a micro-LED array at a plane conjugated to the objective plane. LED arrays are cheap and illumination patterns can be modified at kHz rate [48]. In biological applications to date, the maximum available power is limited [48], and the number of mini-actuators used is generally small (64×64) [48], restraining the number of possible light patterns. However, new developments in microfabrication technologies allow the construction of more powerful high-density micro-LED arrays [49].

Alternatively, digital light processing (DLP) technology can be used as a means of generating and displaying precise spatiotemporal light patterns. DLP was invented by Larry Hornbeck at Texas Instruments in 1987. This is the basis of all the digital projector systems, including those used today to screen motion pictures in the USA. At the heart of this technology lies a digital micromirror device (DMD) which consists of a large number of independently controllable micrometer-scale mirrors (e.g., 1024×768), each one representing one pixel at the sample. A CMOS chip placed underneath each micromirror stores one bit of information (1 or 0) translated into the ON/OFF position. When the DMD chip is illuminated by an external source, the light reflected by each micromirror in the ON position is directed toward the optical path, whereas the light reflected by micromirrors in the OFF position is physically blocked. Each micromirror can be independently switched ON/OFF at microsecond timescale to create arbitrary light patterns. A DMD device can be used to project not only binary patterns, but also graded ones. The brightness of any pixel at the sample can be modulated by the duty cycle (ratio of ON vs. OFF states per unit time) of the corresponding micromirror. For example, in an 8-bit system, one can achieve 255 shades of grey [50].

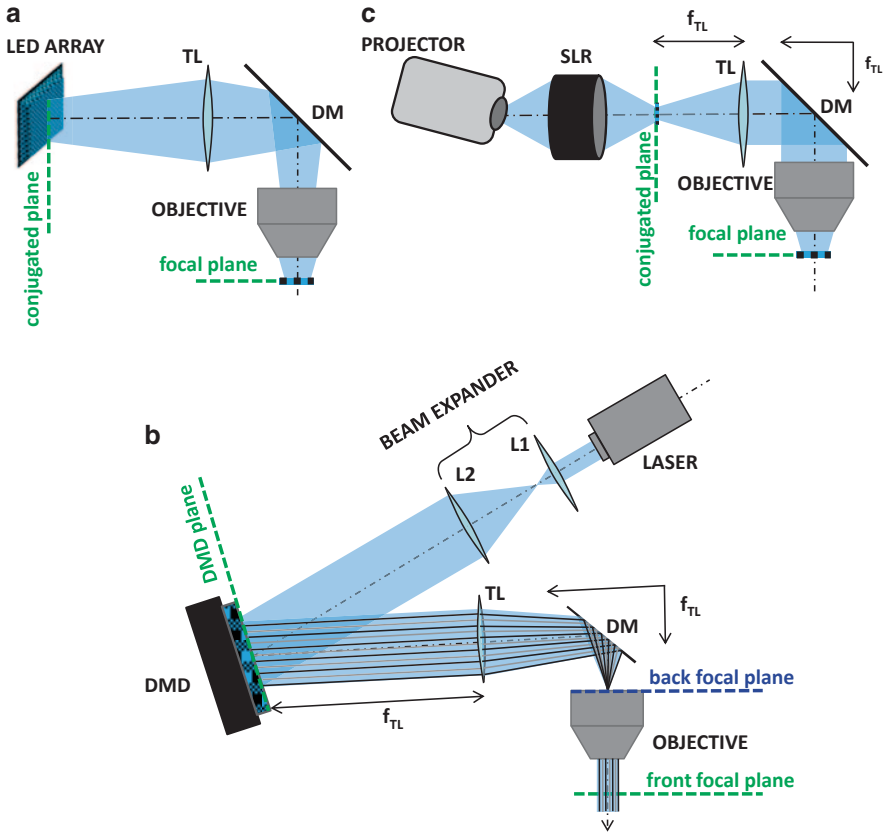


Fig. 9.2 Light patterning by intensity modulation—optical configurations. **a** An LED array is imaged into the sample using a telescope formed by the tube lens (*TL*) and the microscope objective. **b** A beam expander formed by lenses L1-L2 magnifies a laser beam to illuminate the DMD chip. The light reflected by the DMD is projected into the sample via a TL and the microscope objective, resulting in a pencil of parallel light carrying the desired pattern. **c** The output of a DLP projector is imaged onto an intermediate plane using an SLR lens. This intermediate pattern is further imaged into the sample with a telescope formed by the TL and the objective. In all configurations, a dichroic mirror (*DM*) is placed above the objective to rotate the illumination beam so that it impinges perpendicularly onto the back aperture of the objective

9.2.2 Optical Configurations

The LED array/DMD is imaged onto the sample using a pair of lenses (a telescope). Generally, the lens closest to the sample is the objective, while the other one is called the “tube” lens (TL—because traditionally it was placed in a tubular holder) (Fig. 9.2a). A convenient configuration consists in placing the LED array/DMD at the focal plane of the tube lens (i.e., at a distance equal to the tube lens focal length, f_1), while ensuring that the distance between the tube lens and the objective

is the sum of their focal lengths ($f_1 + f_2$). What determines the choice of the lenses? The ratio of the focal lengths (f_2/f_1) is the demagnification ratio and sets the size of the field of stimulation (FoS). Depending upon the desired FoS size and given the focal length of the objective, the required focal length of the tube lens can be calculated using Eq. 9.2:

$$FoS\ size = \frac{f_2}{f_1} Object\ size \quad (9.2)$$

In case of DMD chips, an additional telescope (called the beam expander) is used to bring the LASER/LED light to the DMD and to expand it to match the size of the chip (Fig. 9.2b). Since the intensity of light from extended sources such as arc lamps/LED decreases steeply with distance, it is desirable to place the light source as close as possible to the DMD. This is not necessary if the light source is a collimated laser beam.

Another possible configuration involves a commercial projector, which comes with its own DMD chip along with an internal light source and an output lens (Fig. 9.2c). Since the projector output beam is tilted with respect to the optical axis ($\sim 10\text{--}20^\circ$), the projector should be placed on a stage such as to compensate for this angular displacement and ensure that light comes out parallel to the optical axis. A second lens is further needed to collimate (as much as possible) the beam. Since the projector output beam is highly divergent, it is advisable to place this lens as close as possible to the projector to minimize power loss. Single light reflex (SLR) camera lenses have wide acceptance angles and are therefore ideally suited for such high-divergence conditions. In addition, they are corrected for coma and spherical aberrations, which can otherwise significantly distort the projected patterns. The SLR lens creates an image of the DMD chip at an intermediate position which can be further treated as a new object to be imaged at the sample using a tube lens and an objective as described above (Fig. 9.2c). Within this configuration, it is important to choose the tube lens with a short focal length to minimize light loss due to high divergence. Note that usage of a short focal length tube lens also increases the size of the FoS for a fixed objective. Therefore, a trade-off must be reached between the desired size of FoS and the focal length of the tube lens. To achieve a large FoS, a typical microscope objective can also be replaced with an SLR lens. The temporal resolution is limited by the refresh rate of the projector, usually in the range of 60–360 Hz. In single-chip projectors, rapidly spinning a color wheel to combine appropriate RGB components for each pixel creates the illusion of color to the human eye. To utilize the full refresh rate of single-chip projectors, it is therefore useful to remove the color wheel from the optical path (complete disconnect usually has undesired effects). The output color can be modified for a variety of optogenetic actuators by placing excitation filters in the optical path.

Examples of light patterns obtained with a DMD setup similar to the one described in Fig. 9.2b are shown in Fig. 9.3.

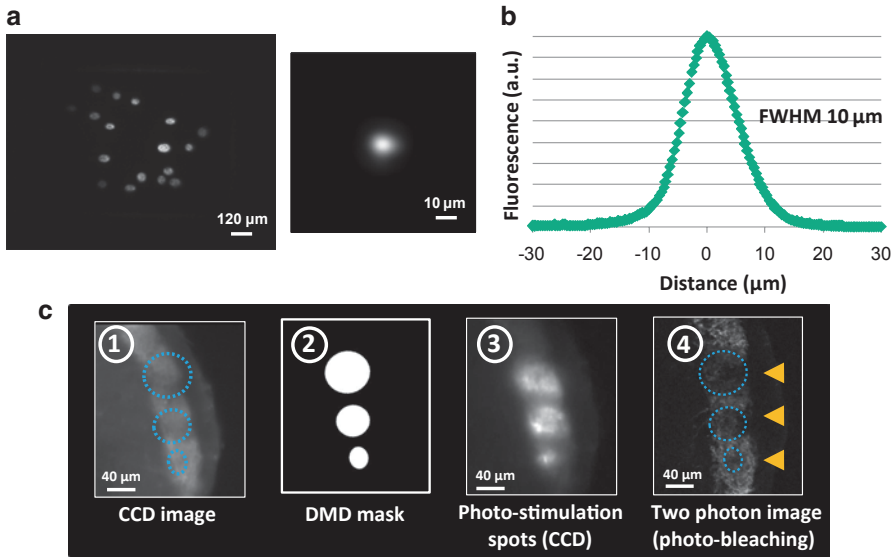


Fig. 9.3 Example DMD patterns. **a** DMD spots reproducing the shape of glomeruli in the olfactory bulb, projected onto a thin ($1\ \mu\text{m}$) fluorescent layer and imaged with a CCD camera. **b** *Left*: image of a $20\text{-}\mu\text{m}$ -diameter spot projected with a DMD. *Right*: Lateral intensity profile for the spot shown on the left. **c** (1–2) Three DMD spots were targeted into the glomerular layer of a sagittal olfactory bulb slice, from a transgenic mouse expressing Chr2-YFP in the olfactory sensory neurons. (3) Wide-field images of the emitted fluorescence from regions in the sample illuminated by the DMD spots. (4) Two-photon image of the same slice: photobleached regions indicate the location of the DMD spots previously shown. Note the precise spatial correspondence between the desired and actual location of the projected photostimulation patterns

9.2.3 Choice of the Light Source

The choice of light source is critical and has important consequences for photostimulation experiments. A simple and cheap solution is to use LEDs (a *noncoherent* source), which come in different colors and have high luminance for effective optogenetic manipulations. Since noncoherent light cannot be perfectly collimated, the effective power decreases steeply with distance from the light source, imposing constraints in the ability to stimulate opsins [26].

Other noncoherent light sources, including the arc lamps found inside projectors, have generally high power and a wide wavelength spectrum, thus permitting multicolor excitation.

If power is still limiting (for example, when photostimulating multiple large regions), lasers can be used as light sources for a DMD. Laser light is coherent and propagates through space with minimal power loss, which makes it possible to place the light source farther from the DMD. Additionally, the photostimulation pattern at the sample has higher contrast between its ON and OFF pixels compared to noncoherent sources. This is due to the fact that it is impossible to focus noncoherent

light from an extended source (such as a lamp or an LED) to a diffraction-limited spot or equivalently to create sharp edges in the pattern. The disadvantage is that laser light will produce higher-order diffraction replicas of the pattern (*ghosts*) from the physical edges of the micromirrors. To get rid of the ghost patterns, a variable aperture diaphragm can be placed in the optical path.

9.2.4 Trade-off Between Field of Stimulation Size and Resolution

The use of a telescope to image the DMD or LED array into the sample determines the size of the FoS, as well as of individual excitation spots (pixels). The latter is defined as the theoretical resolution of the photostimulation system. The size of individual pixels and of the FoS is determined by the ratio of the focal lengths of the objective and the tube lens (demagnification, Eq. 9.2). There is, thus, a trade-off between the maximum size of the FoS and the resolution. For example, let us consider a gallium arsenide LED array (64×64 , $20 \mu\text{m}$ diameter, $50 \mu\text{m}$ spacing) [48] imaged onto the sample with a 1:1 size ratio (using same focal length lenses). This results in an FoS of $\sim 3 \times 3 \text{ mm}^2$. The theoretical resolution in this case is simply the size of an individual LED ($\sim 20 \mu\text{m}$). To obtain a better resolution (e.g., $\sim 2 \mu\text{m}$), the entire LED array needs to be demagnified 10 times at the sample using appropriate lenses, which also results in 10 times smaller size of the FoS ($\sim 0.3 \times 0.3 \text{ mm}^2$). For the same reasons, in case of a DMD, the size of an individual pixel at the sample and the size of the FoS are inversely related. Since DMD devices have large number of micromirrors, it is theoretically possible to have a much smaller excitation spot ($\sim 1 \mu\text{m}$) at a reasonable FoS size ($\sim 1 \text{ mm}$) (Table 9.1). However, in practice, this is a lower bound, since the actual photostimulation resolution is constrained by scattering in the sample.

9.2.5 Applications

Over the past decade, DMDs have been used not only as projection systems, but also in a wide variety of other applications. In epifluorescence microscopes, DMDs have been placed in the illumination path to shape the excitation beam. DMDs have also been integrated in confocal microscopes to achieve spatial discrimination in the absence of a pinhole [51].

Patterned illumination strategies using DMDs for optogenetic stimulation are becoming increasingly popular. Initially, such approaches were successfully used to stimulate light-sensitive ionotropic glutamate receptors in cultured neurons [52] and Chr2-expressing ganglion cells in retinal explants [53]. DMD technology has been used to deliver light to select regions of the spinal cord in zebrafish [54, 55] and in immobilized *C-elegans* [56]. Recently, behavioral tracking of locomoting *C-elegans* was combined with DMD technology to illuminate target sites in a closed-loop design [57, 58].

DMD-based optogenetic stimulation has been effectively combined with neuronal readout methods, such as extracellular or patch clamp recordings. A commercial projector system was used to excite input nodes called glomeruli (one at a time) in the olfactory bulb (OB) of genetically engineered mice that express ChR2 in the terminals of olfactory sensory neurons (OSNs) [59, 60]. Simultaneous extracellular recordings from pairs of output neurons (mitral/tufted cells) enabled the investigation of the interplay between common input and lateral local signals within the circuit [59] and temporal integration rules in different brain regions [60]. In zebrafish, DMD technology coupled to optogenetic activation was used to excite ensembles of mitral cells [61], as well as genetically targeted interneurons in the OB [62]. Varying the distribution of pixels in the ON vs. OFF states (at a carrier frequency of 20 Hz) allowed the manipulation of the synchrony of neuronal ensemble activation. Simultaneous intracellular recordings in a cortical target region allowed them to investigate the role of input synchrony in determining the firing rate/spike timing of target cells [61].

Further, DMD stimulation can be coupled with two photon microscopy to read out activity patterns from a large number of cells as opposed to one or a few cells accessed by electrical recordings (Sect. 9.3.11).

All these studies demonstrate the effectiveness and the potential of using DMD-based approaches for optogenetic manipulation of neuronal ensembles coupled to various readout methods for studying neuronal circuit dynamics.

9.2.6 Limitations

Light propagating deep into biological tissues is subjected to scattering. This is an important constraint for one-photon light patterning techniques (Table 9.1), since scattering deteriorates the spatial precision of stimulation and causes ballistic power loss (that is loss of nonscattered photons). For example, the *mean free path* in brain slices for light of 405 nm is 25 μm [63]. This corresponds to a residual power of <2% at a depth of 100 μm from the surface of the slice. Because of the use of longer excitation wavelengths and its nonlinear nature, two-photon illumination is more resistant to scattering and thus the technique of choice to image and photostimulate deeper in the brain [64, 65]. Unfortunately, two-photon stimulation requires high power exactly due to nonlinear absorption processes. This approach is not compatible with intensity-modulation techniques since light patterning is obtained by blocking the illumination light in pixels corresponding to off-target locations at the sample, which results in substantial power loss. Within these constraints, a more efficient strategy is shaping the illumination such that all available light is redirected toward the targets in the sample. In phase-modulation light patterning techniques, this is achieved by modifying the phase of the illumination light using an SLM device as described in Sect. 9.3.

Table 9.1 Comparison of intensity and phase based patterned illumination techniques

	Intensity modulation techniques	Phase-modulation techniques
Size of FoS	~ several mm ²	<400 x 400 x 400 μm ³ (2p)
Spatial resolution	x-y ~ 1–10 μm; z ~ 1–100 μm	Superior, x-y and z ~ 1 μm (2p)
Tissue axial penetrance	Poor, <100 μm	Superior, <500 μm (2p)
Temporal resolution	60 Hz–5 KHz	Nematic LC-SLM, 60–200 Hz
Number of targets	Tens-hundreds	Few tens (2p)
Coupling to imaging/ ephys readout methods	Easy to implement	Easy to implement

9.3 Light Patterning by Phase Modulation

9.3.1 General Principle

The *phase* of a wave can be defined as the fraction of the oscillation cycle that the wave has travelled at a particular time point. Referring back to Eq. (9.1), describing the electric field oscillating in space at a given time, the phase is given by the angle ψ :

$$E(\vec{r}) = A(\vec{r})e^{i\psi(\vec{r})} \quad (9.1)$$

It is helpful to introduce the concept of *wavefront*, as the spatial envelope of all points where the light electric field has the same phase at a given time. For example, a collimated laser beam has a planar wavefront, since the light electric field at all the points in any plane perpendicular to the direction of propagation has the same phase (Fig. 9.4a). Modulating the phase of a light beam can thus be thought of as changing the shape of its wavefront. This is a recurring event in any optical setup. For example, a lens focusing a collimated laser beam into a point is an SLM that changes a planar wavefront into a spherical one (Fig. 9.4a), while a *diffraction grating* is an SLM that produces a phase gradient equivalent to a tilted wavefront (Fig. 9.4b). The shape of the wavefront impinging on a lens (e.g., on the microscope objective) determines the light distribution beyond that lens. For example, a collimated laser beam (planar wavefront) will be focused at the focal point of the objective. However, a divergent laser beam (convex wavefront) will be focused beyond the focal plane, and a convergent beam (concave wavefront) will be focused before the focal plane (Fig. 9.4c). Introducing a tilt in the wavefront at the back aperture of the objective displaces the focused point laterally in the front focal plane of the objective: the larger the tilt, the bigger the lateral displacement (Fig. 9.4d).

Thus, through simple modifications (curvature, tip, or tilt) of the wavefront shape at the back focal plane of the microscope objective, the intensity distribution can be altered at the sample and the focused laser point can be displaced in 3D. By implementing more elaborate modulations of the wavefront, arbitrary intensity patterns can be obtained, including multiple spots in 2D and 3D, as well as light

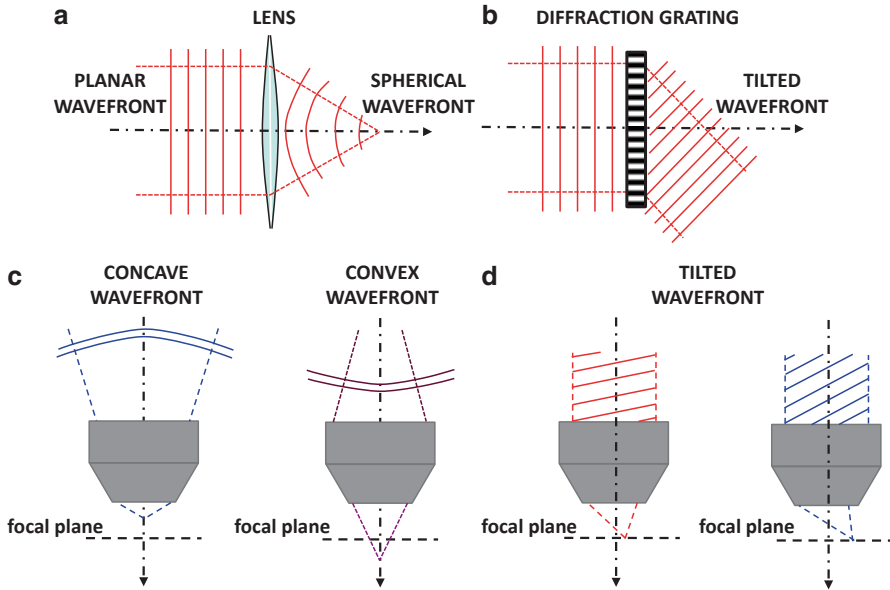


Fig. 9.4 Wavefronts. **a** A planar wavefront propagating parallel to the optical axis is transformed by a lens into a spherical wavefront. The light is focused into a diffraction-limited spot at the focal point of the lens. **b** The propagation direction of a planar wavefront is changed by a diffraction grating. Note that, for simplicity, only the +1 diffraction order is represented. **c** Examples of concave (*left*) and convex (*right*) wavefronts impinging onto the back aperture of a microscope objective. Light is focused by the objective in a point above and below the focal plane, respectively. **d** Example of tilted wavefronts impinging onto the back aperture of a microscope objective. Light is focused into a diffraction-limited spot laterally displaced from the focal point of the objective. A steeper tilt (*right*) causes larger displacement

profiles reproducing the shape of biological objects (i.e., cell bodies, dendritic or axonal branches). This principle constitutes the basis of phase-modulation light patterning techniques such as digital holography [66–68], described in this section.

9.3.2 Optical Configuration

In digital holography, light patterning at the sample is obtained by modulating the phase of a collimated laser beam at the back focal plane of the microscope objective. Since the back focal plane of the objective is not physically accessible, phase modulation is implemented by placing an SLM in a conjugated plane. The SLM is composed of a 2D matrix of ~500,000 liquid crystals, hence its name—liquid crystal spatial light modulator (LC-SLM, Box 2). Each LC-pixel can be independently controlled to introduce a desired phase delay to the incident light. The overall wavefront modulation is the envelope of the individual LC-pixel contributions.

Box 2: Technical Specification of DMD and LC-SLM Chips

Digital Micromirror Device

The digital micromirror device (DMD), as the name suggests, is an array of aluminium micromirrors manufactured by Texas Instruments. It comes in various array sizes such as extended graphics array (XGA, 1024×768), super-extended graphics array (SXGA+, 1400×1050), etc, each micromirror dimension being either 13.7 or 10.8 μm . The reflectivity is usually high for a broad range of visible wavelengths (400–700 nm). Each micromirror can be tilted at an angle of -12° or $+12^\circ$, with respect to the normal (perpendicular to the DMD plane), by a hinge that runs diagonally. Each mirror is electronically controlled to switch between ON ($+12^\circ$) or OFF (-12°) positions independently. A CMOS static random access memory (SRAM) cell underneath each mirror determines the direction of the tilt by electrostatically pulling either of its two free corners. The process of loading the memory cell with a 1 or a 0 is decoupled from the physical movement of the micromirrors, which is synchronized to a separate clock signal. This signal can be applied to specific sectors, or to the whole chip all at once. The optomechanics are robust enough to avoid hysteresis in the movement of the micromirrors. Under normal operation, the mirrors must sit at either of the two tilts and can only return to rest (0°) when the array is set into the “parked” mode. The time it takes for the entire array to refresh is $\sim 150 \mu\text{s}$, making it ideal for fast and precise temporal control. Basic functions to operate the DMD via control boards can be implemented in software available from the manufacturers in conjunction with LABVIEW or C/C++.

Liquid Crystal Spatial Light Modulator

Each pixel in a *liquid crystal spatial light modulator* (LC-SLM) chip is composed of a layer of liquid crystals (LC) sandwiched between the two poles of a transparent electrode. LC are birefringent materials characterized by a molecular anisotropy, resulting in perpendicular axes of symmetry with different associated refractive indices (ordinary and extraordinary): The actual refractive index experienced by light travelling through the LC depends on the relative orientation between these axes and the polarization plane of the incident laser beam [72]. A change in the applied voltage causes the LC molecules to reorient, triggering a change in refractive index.

Since the amount of phase delay experienced by light in a medium is proportional to the refractive index, spatial phase modulation can be achieved by varying the voltage applied within each pixel of the SLM. The relationship

between the applied voltage and the resulting phase modulation (lookup table, LUT) is typical of each instrument and generally provided by the manufacturer. Often, instead of the actual voltage value, the LUT is specified in terms of number of bits (which express the grey levels) sent to the computer interface performing the digital-to-analog (D/A) conversion.

The velocity of re-orientating the LC molecules within each pixel depends on the LC material, on the thickness of the LC layer, and on the type of voltage signal applied to the electrode [72]. These parameters, together with the choice of the D/A interface, determine the maximum refresh rate of the LC-SLM (Sect. 9.3.6).

In reflective LC-SLMs, a dielectric mirror is mounted behind the LC layer. In order to minimize light loss, the reflectivity of the mirror needs to be high (>90%) for the wavelength of interest. This requires the mirror to be appropriately coated. It is possible to coat the mirror with multiple layers in order to achieve high reflectivity for a wider range of wavelengths at the expense of potentially compromising the flatness of the mirror, a key parameter to assure uniform phase modulation across the LC-SLM chip.

A schematic of a typical setup for digital holography is represented in Fig. 9.5. A collimated laser beam is used as the illumination source, to ensure that a planar wavefront impinges onto the SLM plane. The beam is first magnified by a beam expander (L1-L2 in the figure), in order to fully illuminate the LC-SLM chip. The beam is then reflected by the LC-SLM onto a second telescope (L3-L4) that produces an image of the LC-SLM chip in the back focal plane of the microscope objective. This telescope must be aligned in a *4 f configuration*, meaning that its composing elements (LC-SLM, L3, L4, objective back aperture) are at focal distances from one another (Fig. 9.5). This configuration is convenient, since it allows access to two fundamental planes of the optical system: a plane conjugated to the back focal plane of the objective (Fig. 9.5, *blue*), where the LC-SLM chip sits and where the phase modulation occurs, and a plane conjugated to the front focal plane of the objective (the sample plane, Fig. 9.5, *green*). Within this configuration, a real magnified image of the actual pattern projected into the sample is formed around the L3 front focal plane, allowing rapid visual inspection.

9.3.3 Algorithms for Digital Holography

The main goal of digital holography is to establish what phase distribution at the back focal plane of the microscope objective (and hence at the LC-SLM) will result in the desired light intensity distribution into the sample. The back focal plane of the objective (also called pupil plane) sits inside the lens and is not directly accessible, but, for practical purposes, it can be approximated by the back aperture. Determin-

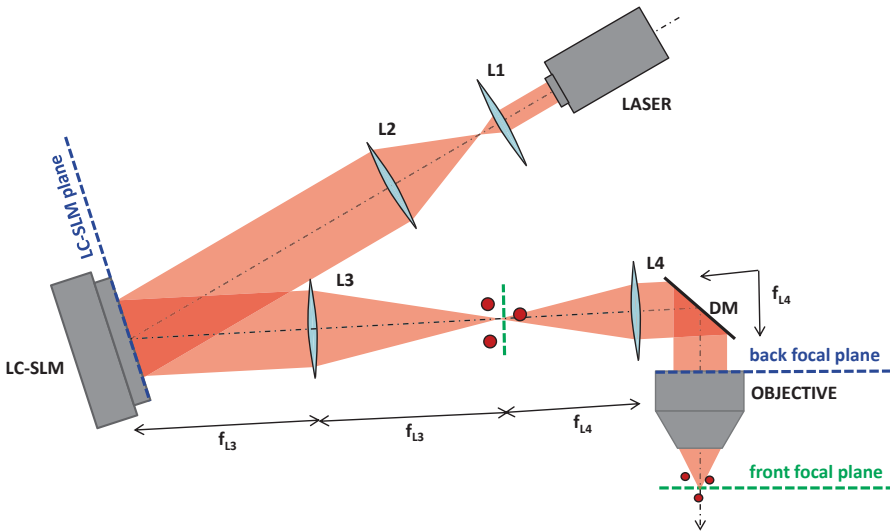


Fig. 9.5 Digital holography—optical configuration. A beam expander formed by lenses L1-L2 magnifies a laser beam to illuminate the LC-SLM chip. A telescope formed by lenses L3-L4 images the LC-SLM chip onto the back aperture (*back focal plane*) of the microscope objective. The objective transforms the phase profile implemented by the LC-SLM into the desired intensity pattern at the sample. Note that a magnified replica of this pattern is formed at the front focal plane of L3. A dichroic mirror (DM) placed above the objective rotates the illumination beam, so that it impinges perpendicularly onto the back aperture of the objective

ing the phase profile at the back focal plane can be solved computationally, and many algorithms have been developed to generate phase profiles (masks) that result in 2D or 3D light patterns of choice. A complete review of these algorithms [69–72] is beyond the scope of this chapter. However, it is important to illustrate some basic strategies which may help the reader understand the physical principles underlying digital holography.

Generating a 3D Distribution of Diffraction-Limited Spots One can place a diffraction-limited spot in 3D by creating an appropriate phase profile at the back aperture of the objective. In order to analytically determine this phase profile, the phase (ψ) at each point of the back aperture needs to be expressed as a function of the spot position in the sample space ($\vec{r}(x_r, y_r, z_r)$). By describing the phase at the back aperture in polar coordinates, ϕ (azimuth angle) and ρ (normalized radius), the phase profile generating the target spot can be written as follows (for derivation, see Botcherby et al. [73]):

$$\psi(\rho, \phi, \vec{r}_p) \approx n \frac{2\pi}{\lambda} \left(x_p \rho \sin \alpha \cos \phi + y_p \rho \sin \alpha \sin \phi + z_p \sqrt{1 - \rho^2 \sin^2 \alpha} \right), \quad (9.3)$$

where λ is the wavelength of the light and $n \cdot \sin \alpha$ is the numerical aperture (NA) of the objective. The lateral displacement of the target spot is controlled by the first

two terms of the equation, which depend on ϕ and describe a tip (x displacement) and tilt (y displacement) in the phase. The axial (z) displacement (lens effect) of the target spot is controlled by the last term in the equation. The electric field generating the target spot can then be obtained by substituting the phase ψ into Eq. (9.1):

$$E_p(\rho, \phi, \vec{r}_p) = A_0 e^{i\psi(\rho, \phi, \vec{r}_p)} \quad (9.4)$$

The principle of superposition of waves allows one to calculate the total electric field resulting in a 3D distribution of multiple spots by simply summing the electric fields corresponding to each independent spot:

$$E_{TOT} = \sum_p E_p = \sum_p A_0 e^{i\psi(\rho, \phi, \vec{r}_p)} \quad (9.5)$$

To reconstruct exactly E_{TOT} at the back aperture of the microscope objective, modulation of both the phase and the amplitude of the electric field is required (Eq. 9.5). However, 3D spot patterns can still be generated by modulating only the phase. An easy way is to calculate E_{TOT} , but consider only the resulting phase modulation as the LC-SLM mask, discarding the intensity component (*superposition of prisms and lenses*) [74]. This algorithm is fast and directs light to the target spots rather efficiently [69]. However, since the algorithm neglects the intensity component, the light distribution among different spots is not uniform, especially if the desired photostimulation pattern contains symmetrical arrangements of spots. Adding a random term to the phase of individual spots improves the uniformity of the intensity pattern in the sample (*random superposition*) [75]:

$$E_{TOT} = \sum_p E_p = \sum_p A_0 e^{i\psi(\rho, \phi, \vec{r}_p)} e^{i\psi_{random}} \quad (9.6)$$

Neuronal targets are often not symmetric, in which case the random superposition algorithm might be good enough for practical purposes. Efficiency and uniformity can be further improved using iterative algorithms, such as *Gerchber-Saxton* [76] and *weighted Gerchber-Saxton* [69, 77], at the expense of computational load.

Generating Arbitrary 2D Patterns When aiming at photostimulating neuronal cell bodies and projections, one needs to generate extended 2D patterns, shaped on the target structures. Creating these patterns by placing multiple individual spots next to each other is computationally expensive [72]. A shortcut has been used for calculating extended patterns in the front focal plane of the microscope objective. This strategy exploits a fundamental property of light diffraction, namely the fact that the light electric field at the back focal plane of a lens is the Fourier transform (FT) of the light electric field at its front focal plane [78]. Knowing the desired intensity distribution at the front focal plane of the microscope objective, it is then possible to

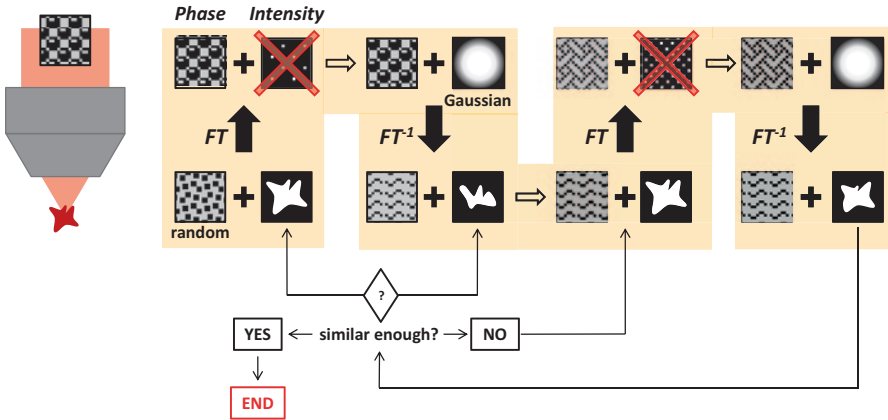


Fig. 9.6 Iterative Fourier transform algorithm (IFTA). Schematic of the IFTA algorithm used to generate 2D holographic patterns, as described in Sect. 9.3.3

derive the corresponding electric field at the back focal plane by simply taking the FT. Importantly, an exact solution of the FT requires modulation of both intensity and phase. One way around this problem is, again, to discard the intensity modulation of the light electric field at the back focal plane of the objective and use an iterative algorithm to generate an optimized phase mask.

An example is the *iterative Fourier transform algorithm* [66, 79], based on the *Gerchber-Saxton routine* [76] (Fig. 9.6). Briefly, an initial electric field is calculated at the front focal plane of the objective, combining the desired amplitude distribution with a random phase:

$$E_0(x, y) = A_D(x, y)e^{i\psi_0(x, y)random} \tag{9.7}$$

A first iteration is performed by:

- a. calculating the FT of E_0 , which corresponds to the electric field at the back focal plane of the objective (as if virtually propagating $E_0(x, y)$ from the front to the back focal plane of the objective):

$$G_0(x', y') = FT E_0(x, y) \tag{9.8}$$

where x', y' are the coordinates for a given point in the back focal plane;

- b. discarding the amplitude of G_0 and substituting it with the amplitude profile of the laser beam impinging on the LC-SLM (generally a 2D Gaussian):

$$G_1(x', y') = A_G e^{i\psi_1(x', y')} \tag{9.9}$$

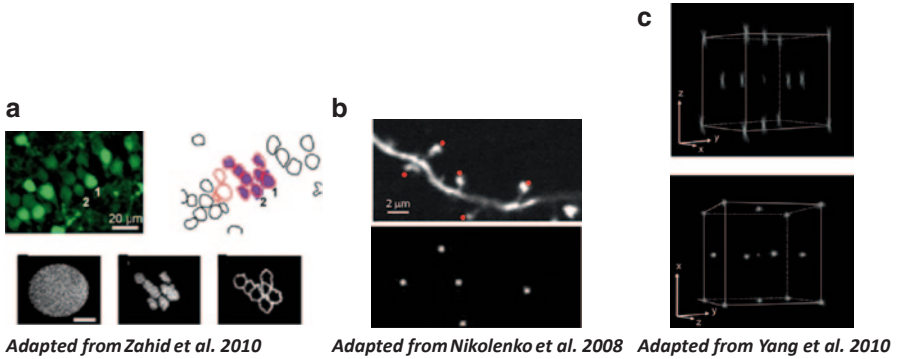


Fig. 9.7 Example holographic patterns. **a** Holographic spots were targeted onto CA1 neurons in a hippocampal slice (*top*). Images of the holographic patterns projected onto a thin (1 μm) fluorescent layer (*bottom*) (Adapted from Zahid et al. [82]). **b** *Top*: two-photon fluorescent image of a dendrite of a pyramidal neuron in a mouse cortical slice. *Red dots* indicate desired positions for the photostimulation spots. *Bottom*: Image of the photostimulation spots generated by digital holography (Adapted from Nikolenko et al. [67]). **c** 3D distribution of holographic spots (*top*: y - z projection; *bottom*: x - y projection) (Adapted from Yang et al. [77])

- c. applying an inverse FT (FT^{-1}) to G_1 , thus obtaining an updated value for the desired electric field at the front focal plane of the objective (as if virtually propagating $G_1(x', y')$ from the back to the front focal plane of the objective):

$$E_1(x, y) = FT^{-1}G_1(x', y') \quad (9.10)$$

The intensity distribution at the sample is calculated as the squared amplitude of $E_1(x, y)$ and then compared with the desired intensity pattern. If the two are sufficiently similar (least square minimization), the algorithm ends here. If further improvement is required, the amplitude of $E_1(x, y)$ is discarded and substituted with the desired amplitude distribution, while the phase is conserved:

$$E_2(x, y) = A_D(x, y)e^{i\psi_1(x, y)} \quad (9.11)$$

A *second iteration* cycle begins. The algorithm rapidly converges to an optimal solution, after ~ 8 iterations [66].

Examples of 2D and 3D patterns obtained by the algorithms described above and imaged on a thin fluorescent cover slip are shown in Fig. 9.7.

9.3.4 Resolution and Precision of Stimulation

In intensity modulation techniques, theoretical resolution is determined by the size of the micromirror in a DMD, or miniaturized light source in an LED array im-

aged at the sample. This one-to-one correspondence between SLM actuators and illumination pixels in the sample is lost in digital holography, where the LC-SLM is placed in a plane conjugated to the back focal plane of the microscope objective. As a result, the light diffracted by every actuator (pixel) of the LC-SLM contributes to all points of the pattern in the sample.

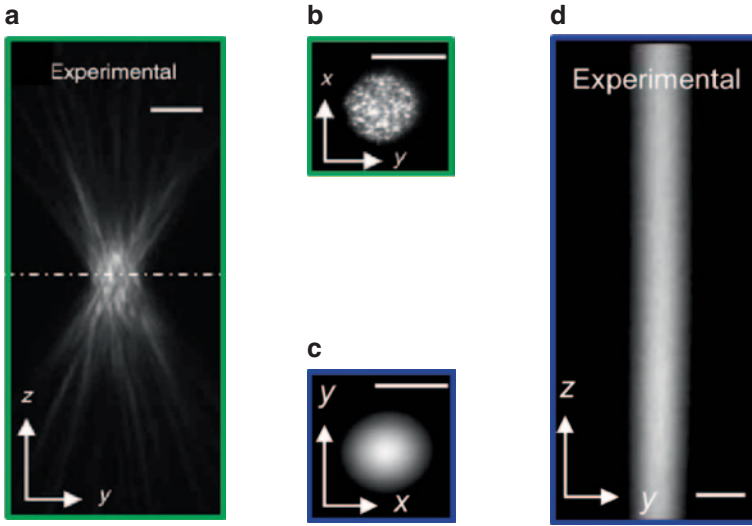
The theoretical resolution of a digital holography system is generally defined as the size of the smallest diffraction-limited spot generated at the front focal plane of the microscope objective. This, in turn, is determined by the numerical aperture (NA) of the objective. Specifically, if the back aperture of the objective is completely filled by the holographic beam, the resolution is equal to the objective resolution (Abbe limit) at the chosen illumination wavelength, just as in imaging systems:

$$x_{min} = y_{min} = \frac{0.61\lambda}{NA} \quad \text{and} \quad z_{min} = \frac{2\lambda n}{NA^2}, \quad (9.12)$$

where λ is the wavelength of the illumination light, NA is the numerical aperture of the microscope objective, and n is the refractive index. In experimental configurations where the back aperture of the objective is underfilled, the resolution depends on the actual numerical aperture ($NA = f_{obj}/r$, where f_{obj} is the focal length of the objective and r is the radius of the holographic beam at the back aperture).

To maintain maximum resolution when placing spots in 3D, it is important to take into account spherical aberration. Indeed, microscope objectives perform as ideal (aberration free) imaging systems only at the focal plane (sine configuration), while the image (in this case the holographic pattern) is rapidly degraded by spherical aberration as it is displaced away from the focal plane [73]. Luckily, it is possible to use the LC-SLM to compensate for spherical aberration [77, 80].

Note that in digital holography, extended spots are generated by shaping the illumination wavefront (iterative Fourier transform algorithm), without underfilling the back aperture of the microscope objective. This results in an improvement of both lateral and axial precisions with respect to spots of the same size obtained by underfilling the back aperture of the objective with a Gaussian beam (Fig. 9.8) [66]. For example, for a 0.8 NA objective, the axial resolution (measured as full-width half maximum of the light intensity profile) of a holographic spot scales as $2\times$ the diameter of the spot (as opposed to the square of the diameter for *Gaussian spots*) [66]. The precision further improves in two-photon photostimulation (Sect. 9.3.7), due to nonlinear effects and the axial resolution (for similar NA objective) is comparable to the spot diameter [81]. For currently available opsins and caged compounds, a single-cell body can be efficiently stimulated with a spot of 10–15 μm diameter [66, 82–84], which corresponds to an axial precision of 20–30 μm or 10–15 μm for one-photon and two-photon digital holography, respectively. In many cases, this precision is sufficient for simulation of single cells, when working at a minimum (but reliable) light power regime [66, 82].



Adapted from Lutz et al. 2008

Fig. 9.8 z-profile of holographic spots. Images of a holographic (a, b) and a Gaussian spot (c, d) of the same diameter. Lateral (b, c) and axial projections are compared (Adapted from Lutz et al. [66])

9.3.5 Trade-off Between FoS Size and Resolution

In digital holography, the FoS cannot be thought of simply as a scaled version of the LC-SLM chip. However, a relationship between the size and number of the LC-SLM pixels and the extent of the FoS can be derived following the laws of diffraction.

For determining the 2D FoS, one can exploit, once again, the fact that the front and back focal planes of the objective are related by an FT. A first step is to calculate the actual electric field at the back focal plane, which is the electric field at the LC-SLM, spatially magnified by a telescope (L3-L4 in Fig. 9.5). This electric field can be described as the continuous holographic profile broken up into discrete units, each corresponding to individual pixels of the LC-SLM (Fig. 9.9a). Mathematically, the LC-SLM chip imaged in the back aperture of the objective is represented as the convolution of a *comb function* with periodicity equal to the interpixel distance and a *rectangular (rect) function* representing the shape of individual pixels. These functions, when multiplied by the electric field corresponding to the holographic phase profile, give the actual electric field at the back focal plane of the objective.

The second step consists in propagating the discretized electric field thus calculated to the front focal plane by inverse FT. The result is illustrated in Fig. 9.9b: note how FT converts multiplications into convolutions and vice versa. Importantly, the resulting light pattern at the front focal plane of the objective is filtered (convolved)

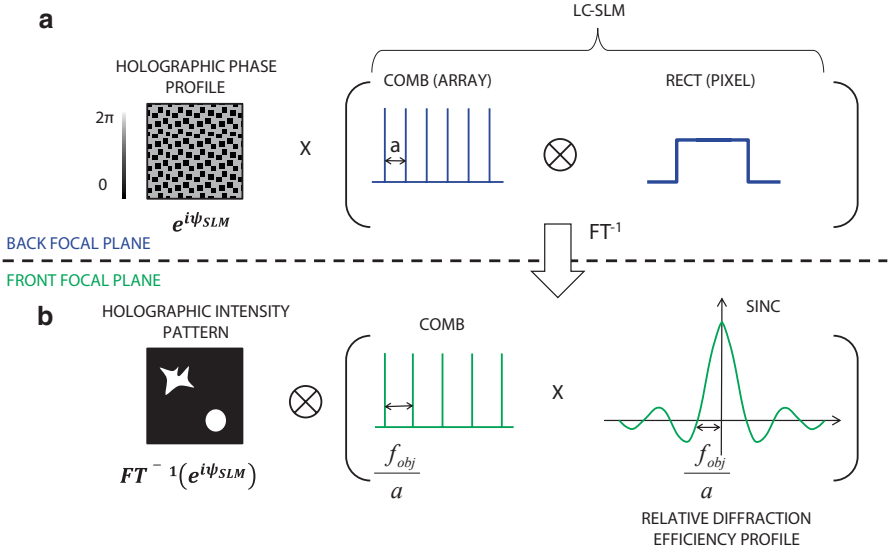


Fig. 9.9 Inverse Fourier transform of the light electric field between the back and the front focal plane of the objective in digital holography. **a** Back focal plane: The image of the LC-SLM at the back focal plane of the objective is the convolution of a comb function with periodicity equal to the interpixel distance, and a rect function representing the shape of an individual pixel. This function is multiplied by the electric field corresponding to the holographic phase profile. **b** Front focal plane: The inverse Fourier transform (FT^{-1}) performed by the objective converts convolution into multiplication and vice versa. As a consequence, the desired holographic intensity pattern is convolved by the product of a comb function with a sinc function (FT^{-1} of the LC-SLM comb function and the pixel rect function, respectively). Ψ_{SLM} : phase profile at the LC-SLM/back focal plane; a : pixel size at the back focal plane; λ : wavelength of the illumination light; f_{obj} : focal length of the microscope objective

by a sinc function arising as the inverse FT of the pixel rect function. This transformation results in an inhomogeneous, bell-shaped lateral intensity profile of the following form [71, 77]:

$$\frac{I_{spot}}{I_0} = \left(\frac{\sin x^*}{x^*} \right)^2 \left(\frac{\sin y^*}{y^*} \right)^2, \text{ with } x^* = \left(\frac{\pi a}{\lambda f_{obj}} x \right) \text{ and } y^* = \left(\frac{\pi a}{\lambda f_{obj}} y \right) \quad (9.13)$$

(I_{spot} : intensity of a holographic spot at any location in the focal plane of the objective; I_0 : intensity of a spot at the focal point of the objective; a : size of the image of one pixel of the LC-SLM at the back aperture of the objective; f_{obj} : focal length of the objective; x, y : coordinates at the sample plane).

The ratio (I_{spot}/I_0) is referred to as relative diffraction efficiency of the system. Most of the available power (>90%) is contained in the first order of the sinc function, whose first zero values at $x_0 = y_0 = \lambda f_{obj}/a$ define the accessible FoS. In many applications, the FoS is further limited to the region where relative diffraction

efficiency is $\geq 50\%$, which ensures higher uniformity of intensity and avoids ghost spots (Sect. 9.3.8).

Note that the extent of the illumination field is inversely proportional to the size of the LC-SLM pixel imaged at the back focal plane of the objective. As a consequence, the resolution and extent of the FoS are not independent. In fact, maximal resolution requires that the image of the LC-SLM chip fills the back aperture of the objective. For a given number of pixels in the chip of the LC-SLM, this sets the size of the pixel imaged at the back aperture (a) and thus the extent of the FoS. Larger FoS can be obtained by underfilling the back aperture (smaller a), at the expense of resolution.

In the axial direction, the relative diffraction efficiency also decreases as the stimulation point is moved away from the focal plane of the objective [71, 77]. Indeed, the LC-SLM behaves as a diffraction grating of periodicity equal to the interpixel distance. Light diffracted from a single LC-SLM pixel propagates from the pupil of the objective to the sample within a cone of half angle $\theta = \lambda/2a$. This limits the extent of the axial region illuminated by LC-SLM pixels imaged at the border of the objective back aperture and causes a decrease in relative diffraction efficiency for points farther away from the focal plane [77]. The maximal achievable axial displacement of a holographic point is limited by the numerical aperture of the microscope objective to $\sim \lambda n f_{obj} / 2aNA$ [72, 77]. The bell-shaped profile of the relative diffraction efficiency can be computed numerically, by adding the contribution of all LC-SLM pixels to a stimulation point in the sample at different positions along the optical (z -) axis [77].

As an example, for an illumination wavelength of 1060 nm, considering a typical pixel size at the back focal plane of the objective of $\sim 20 \mu\text{m}$ and a $20\times$, 1.0 NA objective with focal length 9 mm, the 3D FoS of digital holography is $\sim 400 \times 400 \times 400 \mu\text{m}^3$ (Table 9.1).

9.3.6 Dynamical Alternation of Patterns

Different phase profiles can be sequentially displayed by LC-SLMs, resulting in dynamical alternation of light patterns at the sample. However, the refresh rate is limited by the response time of the liquid crystals (LC), the properties of the electronic circuit driving the chip, and the type of interface between the LC-SLM and the computer.

Different types of LC have specific response times. Ferroelectric LCs can alternate phase profiles at KHz rates, but they are limited to a binary phase modulation [85]. This greatly reduces diffraction efficiency (to a theoretical upper limit of 40% and often a lower actual value) [71].

Nematic LCs are more commonly used to build LC-SLMs for digital holography, since they allow finer phase modulation (typically 8-bit, 256 values for a full 2π phase modulation) and better diffraction efficiency ($> 85\%$, for a diffraction-limited point near the center of the FoS) [85, 86]. However, their increased viscosity

reduces the response time by an order of magnitude. Moreover, both the response time and the maximum amount of phase delay introduced by a nematic LC-SLM are proportional to the thickness of the LC layer. Reflective LC-SLMs, where incident light travels twice through the LC layer, are almost always preferred to transmission ones, since they allow a better compromise between the maximum phase delay and the refresh rate [70]. Nematic LC-SLM models available on the market (Hamamatsu, Boulder) have refresh rates on the order of 60 Hz, if coupled to a DVI computer interface, and > 100 Hz (Table 9.1) with a PCIe interface. Phase profiles can generally be pre-calculated and loaded into the interface, while the timing of presentation is controlled by an internal clock.

9.3.7 Two-Photon Digital Holography

The basic alignment of a digital holography setup does not change between one-photon and two-photon systems, apart from the need for specific reflective coatings on the LC-SLM and the other optical elements (lenses, mirrors), which should match the appropriate wavelength range.

Effects of scattering on two-photon excitation of a small diffraction limited spot have been extensively characterized in the framework of two-photon imaging [65, 87, 88] and are mostly limited to loss of ballistic power. Recent work also explored the propagation of holographic patterns deep into brain tissue. Experimental data and computer simulations showed that holographic patterns are more robust to scattering than Gaussian spots of comparable size and maintain their x–y spatial coherence, as well as z-confinement up to a depth of ~ 250 μm ($\lambda = 800$ nm) [84, 89]. The robustness to scattering is due to the much broader angular spectrum (i.e., spatial frequency) content of a holographic beam compared to a low-NA, Gaussian beam, which must underfill the back aperture of the objective in order to generate a spot of comparable size. The broad angular content makes the holographic beam less sensitive to small perturbations in spatial frequency induced by scattering in the tissue, allowing nearly undistorted propagation of the holographic pattern. The depth penetrance of holographic beams can be further increased (up to 500 μm , Table 9.1) by coupling digital holography with temporal focusing [81, 84, 90, 91].

Temporal focusing [90, 91] utilizes a diffraction grating to disperse the spectral components of the laser pulse, thereby widening the temporal profile of the illumination beam. The separated frequencies travel different paths through the tissue and recombine only in the front focal plane of the objective. As a result, the laser pulse reaches its minimum duration only in the focal plane allowing maximal probability for two-photon absorption. This confines the two-photon excitation to a few micrometers (~ 5 μm) [81] above and below the focal plane, significantly improving the z-confinement of the holographic pattern. Temporal focusing also improves the spatial homogeneity of the holographic pattern when propagating through scattering samples [84, 89]. Importantly, while temporal focusing allows deeper penetration, it is associated with power loss at the diffraction grating ($\sim 20\%$). Therefore,

when implementing this strategy, power loss due to the combined effects of optics and scattering must be first characterized in order to estimate the number of targets that can be modulated optically in the deep layers.

One disadvantage of two-photon versus one-photon excitation is the higher power requirement, due to the dependence of two-photon absorption probability on the squared intensity of the illumination light. This limits the number of targets that can be stimulated simultaneously by two-photon digital holography. In digital holography, the available power is split among the illuminated spots, proportionally to their area. Thus, for a constant illumination power, the intensity in a circular area of radius R will be about fourfold lower than that in a spot of radius $R/2$, and the two-photon absorption probability will decrease by 16-fold. On the other hand, larger spots are often more efficient at stimulating neurons. Opsins such as Channelrhodopsin 2 (ChR2) have a relatively large two-photon *cross-section*, but a low single-channel conductance [45]. Thus, a neuron expressing ChR2 is optimally activated by a low-intensity ($>0.2 \text{ mW}/\mu\text{m}^2$) spot, covering the entire cell body [83, 84]. 2D extended patterns can be used to activate multiple neurons simultaneously, with stimulation pulses of a few milliseconds [84, 89, 92].

An alternative solution is to rapidly scan a small diffraction-limited two-photon excitation spot across a neuronal cell body, recruiting multiple opsin molecules sequentially [45]. This approach is particularly efficient for ChR variants with increased single-channel conductances and longer off-time kinetics [93, 94]. In one implementation of this strategy, a 3D distribution of diffraction-limited holographic spots is generated to target multiple neuronal cell bodies. The holographic beam is then scanned by galvanometric mirrors, such that all the spots are simultaneously steered through the target cell bodies. This approach has the potential to allow simultaneous activation of a larger number of cells, at the expense of longer simulation times (tens of milliseconds, with the currently available ChR variants) [93].

To date, a study assessing the maximum number of neurons that can be activated simultaneously by two-photon digital holography is still lacking. Given currently available laser technology, opsin variants, and constraints imposed by tissue photodamage, a reasonable estimate for the number of neurons that can be simultaneously modulated using two-photon digital holography is in the range of a few tens [47, 84, 93].

9.3.8 Caveats

Zeroth Diffraction Order and Ghost Spots The LC-SLM behaves as a diffraction grating. As such, it modulates a fraction of the incident light to form a first diffraction order (the desired spot pattern). However, an important fraction of incident light, corresponding to the constant component of the electric field (zeroth diffraction order), remains unmodulated and is focused into a diffraction-limited spot at the sample. Yet another fraction of the incident light is lost as ghost spots, fainter replicas of the desired spot pattern.

There are two sources of ghost spots. One set of ghosts is generated by the phase-only modulation algorithm, as higher harmonics (higher diffraction orders) of the basic frequency in the LC-SLM diffraction grating. Another set of ghosts results from the pixelated nature of the LC-SLM (Fig. 9.9). At the front focal plane of the objective, a replica of the spot pattern is generated periodically due to the convolution of the spot pattern with the comb function arising from the pixelated nature of the LC-SLM. The period of these ghost spots is given by $\lambda f_{obj}/a$ (a , SLM pixel size imaged at the back aperture of the objective) and is equal to the half-width of the bell-shaped relative diffraction efficiency profile (Sect. 9.3.5, Eq. 9.13). Hence, by reducing the effective FoS ($FoS=2\lambda f_{obj}/a$) by half, these ghosts spots can be prevented from reaching the sample [71]. This can be easily achieved by placing a variable aperture diaphragm in a plane conjugated with the sample plane (e.g., focal plane of L3, Fig. 9.5). In the same plane, it is convenient to insert a small block (as simple as a black-painted aluminium foil glued on a glass cover slip) to mask the focused zeroth-order component [66]. If blocking part of the field of view to eliminate the zeroth-order and the undesired diffraction components is not feasible, alternative strategies can achieve the same effect [71, 82, 95]. Finally, an appropriate choice of the LC-SLM helps reduce the amount of light directed into the zeroth-order and ghost spots (Sect. 9.3.9). Corrections to the basic digital holography algorithms discussed in Sect. 9.3.3 also improve efficiency in directing light toward the desired spots [69, 70, 86].

High Frequency Spatial Intensity Inhomogeneities Figures 9.7 and 9.8 show examples of extended 2D holographic patterns, imaged on a thin fluorescent layer. It is immediately apparent that the intensity of the patterns is not homogeneous, but rather characterized by high-frequency inhomogeneities (speckles). The origin of speckles is the IFTA algorithm used to generate the holographic patterns (Sect. 9.3.3), since the phase at the front focal plane of the objective is treated as a free parameter. As a consequence, overlapping points in the pattern can have completely different phases, interacting constructively (bright speckles) or destructively (dark speckles) [96]. The effect is particularly evident for two-photon excitation, given that the quadratic dependence of the emitted fluorescence on the light intensity accentuates the brightness differences between neighboring speckles.

Speckle patterns are generally only a minor problem for photostimulation experiments, because diffusion of the active molecules in the extracellular and intracellular space (caged compounds), or horizontal diffusion in the cellular membrane (optogenetic actuators), even out any inhomogeneities in the illumination profile. Smoother patterns may however be desirable for targeting smaller structures (average dendrite width is comparable to the diameter of a single speckle) and in cases when light patterning by phase modulation is used for optical imaging experiments. Indeed, smoother patterns can be achieved using modified digital holography methods [79, 96–99] or other phase-modulation techniques such as generalized phase contrast [100, 101].

9.3.9 Tips for Practical Implementation

Choice of the Light Source Unlike intensity modulation, phase-modulation light patterning techniques require the use of coherent light sources (laser illumination), which generate a planar wavefront, allowing effective phase modulation unattainable via incoherent light sources. For the same reason, phase-modulation techniques cannot be coupled with light guides that do not preserve phase information (such as many optical fibers).

For one-photon stimulation, relatively cheap lasers producing a 50–100 mW continuous output can be used. In two-photon digital holography, femtosecond oscillators should be used. The probability of two-photon absorption is proportional to the peak light intensity [64], so this parameter (together with photodamage) ultimately determines the maximum number of targets that can be stimulated simultaneously. Titanium–sapphire lasers have been effectively used for multipoint photo-uncaging [67], but their power decreases steeply at wavelengths >950 nm. For red-shifted optogenetic actuators, single-line femtosecond oscillators [93] and regenerative amplifiers [102] are more powerful choices.

Choice and Alignment of the LC-SLM The choice of the LC-SLM, as well as its characterization and alignment, is critical to a successful implementation of digital holography.

One important characteristic of the LC-SLM is the diffraction efficiency, calculated as the percentage of the incident light that is redirected to the first diffraction order (useful signal). For fine phase modulation, it is key to achieve good diffraction efficiency. In this respect, nematic LCs allowing multilevel phase modulation are preferable to binary ferroelectric LCs (Sect. 9.3.6). In addition, the actual number of achievable phase levels depends on the type of digital–analog interface (8-bit or 16-bit). The shape of the lookup table (LUT, Box 2) also influences the degree of phase modulation, a linear LUT being preferable to a nonlinear one. Another important parameter is the fill factor of the LC-SLM chip, accounting for the space between the LC pixels, where no phase modulation occurs.

If high diffraction efficiency is critical for the success of an experiment, more advanced characterization of the LC-SLM may be required. Measuring a regional LUT (within different sectors of the LC-SLM) can help compensate for inhomogeneous phase modulation across the LC-chip [85]. Furthermore, it is convenient to use a wavefront analyzer to measure the actual phase of the holographic beam when a flat phase profile is applied to the LC-SLM. If any distortion of the wavefront is observed, a compensatory mask can be applied to the LC-SLM [82]. Finally, diffraction efficiency can be improved by compensating for the electrical crosstalk between adjacent pixels [86].

For experiments targeting multiple neurons in a circuit, a large FoS is convenient. In this scenario, LC-SLMs with a larger number of pixels allow for a better compromise between the extent of the FoS and the resolution (Sect. 9.3.5).

Choice of the Lenses In digital holography, the choice of lenses focal length determines the performance of the setup in terms of available power at the sample, quality of resolution, and extent of the FoS. A first telescope (L1-L2 in Fig. 9.5) is used to expand the laser beam impinging on the LC-SLM. The best configuration for uniform illumination is to choose the telescope magnification such that the beam slightly overfills the longer dimension of the LC-SLM chip. The choice of the second telescope, imaging the LC-SLM into the back aperture of the microscope objective, is more critical, since it sets the trade-off between resolution and FoS (Sect. 9.3.5): Overfilling the back aperture assures maximum resolution, while underfilling it allows for a larger FoS.

Integrating Digital Holography Setup in Commercial Systems Digital holography can be assembled in a custom-made setup, but is also easily coupled into commercial microscopes. For this purpose, it is convenient to mount the holographic setup (Fig. 9.5) horizontally on a breadboard, at a height slightly above the back aperture of the objective. A dichroic mirror can be used to rotate the horizontal holographic beam by 45° , so that it impinges vertically on the back aperture of the objective. In upright microscopes, a dichroic module can be mounted right below the epifluorescence arm [66]. Alternatively, the imaging tube lens of the microscope can be used as the last lens of the holographic setup (L4). This imposes some additional constraints on the choice of focal lengths for the other lenses in the setup. Moreover, the user should make sure that the tube lens is placed at a distance from the back aperture of the objective equal to the focal length of the tube lens itself (which is not always the case in commercial systems).

Combining Digital Holography and Imaging The easiest configuration is to implement 2D digital holography and imaging in the same plane [82, 103]. This is achieved by coupling both the imaging and the photostimulation light paths onto the same microscope objective. The two paths can use different light wavelengths, which can be combined with a dichroic mirror above the microscope objective. Alternatively, if the absorption spectra of photosensitive actuators are compatible and the available power is sufficient, the same laser source can also be split between the imaging and digital holography paths. For example, polarizing beam splitters can be used for both separating and recombining the two illumination lines.

In neuronal circuits where the input and the output layers are well defined, it is possible to use digital holography to stimulate in one layer, while imaging in another layer [47]. Generally, the imaging plane is defined by the axial position of the microscope objective through focusing (moving the objective) and coincides with the focal plane of the objective itself. In order to displace the photostimulation pattern to a different plane, a curvature can be introduced in the phase pattern at the LC-SLM to compensate for the axial movement of the objective [104]. If an LC-SLM is introduced in the imaging laser path, the same method can be used to displace the imaging plane, without changing the axial position of the objective [105, 106]. Thus temporally, this approach is not limited by the inertia of the objective, but only by the refresh rate of the LC-SLM (> 100 Hz). Moreover, the use of a LC-SLM allows compensating for spherical aberration that would otherwise deteriorate the image

quality. Remote focusing [73, 80, 107] is an alternative aberration-free method that can be used to modify the imaging plane (by axial shift or tilt) without moving the principal microscope objective.

Introducing a variable wavefront curvature selectively in the imaging path could potentially be also achieved using a deformable mirror [108], a variable focus lens [109, 110], or acousto-optical deflectors [31, 44, 111].

Note that these methods are also compatible with intensity modulation techniques (Sect. 9.2).

9.3.10 Applications

Digital holography was first used in biology in the context of optical tweezers [68, 112]. Here the electric field generated by focused light beams is used to “trap” and manipulate microscopic particles and microspheres, as well as viral particles and bacteria. The first implementation of digital holography created multisite 3D light traps [68, 112]. Later, the technique was used in neuroscience, where simultaneous illumination of extended 2D patterns or multiple spots in 3D allowed multisite neurotransmitter uncaging [66, 67]. The ability of digital holography to generate extended 2D light patterns was exploited to target individual [66] and multiple [82, 103] neurons simultaneously in brain cell cultures and slices, as well as neuronal compartments, such as dendritic branches [66]. Fast holographic illumination was also applied to photostimulate retinal ganglion cells in genetically or pharmacologically blind retinas [113]. Recently, focal 3D multipoint uncaging was used to study dendritic integration and neuronal signal propagation [80, 114, 115].

Importantly, almost from the start, digital holography was extended to two-photon illumination allowing patterned photostimulation in scattering brain samples [67, 81]. Preliminary studies on two-photon stimulation of ChR-expressing neurons in brain slices [84, 93] open exciting venues for future *in vivo* applications. Finally, digital holography is not limited to photostimulation experiments, but it has also been successfully implemented for multiplexed two-photon imaging [67, 103, 105, 116, 117].

Despite these exciting developments, the potential of light patterning by intensity or phase modulation in neuroscience remains vastly unexplored. Further developments will benefit from reducing the gap between developers and endusers and from pursuing a systematic approach to iteratively test, adapt, and optimize these novel techniques by going back and forth between the optical bench and “real-life” experiments in slice preparations, anesthetized and awake behaving animals.

Acknowledgement We would like to thank Aurélien Bègue, Adriana ‘Dăbâcan’, Priyanka Gupta, and Matthew Koh for constructive critique and comments. This work was supported by an EMBO Long-Term Fellowship and a Swartz Foundation Fellowship (FA), and CSHL start-up funds and a Louis and Gertrude Feil Foundation Fellowship (DFA).

Glossary

1. *4f configuration*: an optical configuration involving two lenses of focal length 'f'. The object is placed at focal length distance from the first lens and the distance between the two lenses is 2f. This configuration ensures that the distance between the object and its image is 4f. Even when two lenses of different focal lengths are used (f1 and f2), the configuration is still commonly referred to as a 4f. system.
2. *Absorption cross-section*: a proportionality constant that determines the probability of a photon being absorbed by an absorber molecule. It has the units of area, which is why it is known as cross-section and can be imagined to be a perfectly absorbing disk of that area.
3. *Collimated beam*: a beam of light with near-zero divergence that propagates through a given medium. Lasers are highly collimated, but light from extended sources like lamps and LEDs is not.
4. *Comb function*: a periodic function composed of individual delta functions repeated at a particular interval. Also known as impulse train or sampling function in engineering. The Fourier transform of the comb function is another comb function with different periodicity.
5. *Conjugate plane*: if all points residing in a given plane P are imaged onto another plane P' by a lens, then P and P' are said to be conjugate planes of each other. In an optical system with more than one lens, changes in the amplitude or phase at any given plane propagate to all other conjugated planes.
6. *Diffraction grating*: an optical component with periodic variation of phase across the surface that causes constructive/destructive interference to produce characteristic diffraction patterns.
7. *Diffraction-limited spot*: the theoretical minimum spot size that can be achieved after focusing a coherent light beam using a lens. The size of the spot at the focal plane is proportional to the wavelength of light and inversely proportional to the numerical aperture of the lens. The function that describes the intensity distribution of a diffraction-limited spot in 3D is known as the point-spread function.
8. *Focal plane*: the point where rays parallel to the optical axis converge after passing through a lens is called the focus. The plane perpendicular to the optical axis containing the focus is called the focal plane (technically the front focal plane). Back focal plane refers to the image plane of an object placed at infinity and is located at a focal distance from the center of the lens, but symmetrically opposite from the front focal plane.
9. *Gaussian spot*: a spot generated by a Gaussian beam when focused, whose intensity profile can be fitted with 2D Gaussian function in the lateral plane.
10. *Ghost-replicas*: the higher-order diffraction patterns (low-intensity repeats) of a light mask when using a coherent light source.

11. *LED (Light-emitting diodes)*: a small semiconductor device made up of a pn-junction diode that emits photons (whose energy correspond to the band gap) when an electric potential is applied.
12. *Mean free path*: the average distance travelled by light (photons) between successive collisions (scattering) in the propagating medium.
13. *Rectangular (rect) function*: a step function of a particular duration. Its Fourier transform is a sinc function, whose un-normalized form matches the diffracting pattern from a single-slit (rect function) experiment.
14. *Temporal coherence*: two waves are coherent if they have a constant phase difference between them. For light sources, it is a condition where all the individual light emitters (electron transitions in atoms at the source) have a constant phase difference between themselves, as is the case of LASERS.
15. *Wavefront*: the spatial envelope of all the points in a wave that have the same phase.

References

1. Yuste, R., Konnerth, A., & Masters, B. R. (2006). Imaging in neuroscience and development, a laboratory manual. *Journal of Biomedical Optics*, *11*, 019902.
2. Looger, L. L., & Griesbeck, O. (2012). Genetically encoded neural activity indicators. *Current Opinion in Neurobiology*, *22*, 18–23.
3. Stosiek, C., Garaschuk, O., Holthoff, K., & Konnerth, A. (2003). In vivo two-photon calcium imaging of neuronal networks. *Proceedings of the National Academy of Sciences of the United States of America*, *100*, 7319–7324.
4. Minta, A., Kao, J. P. Y., & Tsien, R. Y. (1989). Fluorescent indicators for cytosolic calcium based on rhodamine and fluorescein chromophores. *The Journal of Biological Chemistry*, *264*, 8171–8178.
5. Hochbaum, D. R., et al. (2014). All-optical electrophysiology in mammalian neurons using engineered microbial rhodopsins. *Nature Methods*, *11*, 825–833. doi:10.1038/nmeth.3000.
6. St-Pierre, F., et al. (2014). High-fidelity optical reporting of neuronal electrical activity with an ultrafast fluorescent voltage sensor. *Nature Neuroscience*, *17*, 884–889.
7. Jin, L., et al. (2012). Single action potentials and subthreshold electrical events imaged in neurons with a fluorescent protein voltage probe. *Neuron*, *75*, 779–785.
8. Trachtenberg, J. T., et al. (2002). Long-term in-vivo imaging of experience-dependent synaptic plasticity in adult cortex. *Nature*, *420*, 788–794.
9. Grutzendler, J., Kasthuri, N., & Gan, W. B. (2002). Long-term dendritic spine stability in the adult cortex. *Nature*, *420*, 812–816.
10. Svoboda, K., Denk, W., Kleinfeld, D., & Tank, D. W. (1997). In vivo dendritic calcium dynamics in neocortical pyramidal neurons. *Nature*, *385*, 161–165.
11. Helmchen, F., Svoboda, K., Denk, W., & Tank, D. W. (1999). In vivo dendritic calcium dynamics in deep-layer cortical pyramidal neurons. *Nature Neuroscience*, *2*, 989–996.
12. Euler, T., Detwiler, P. B., & Denk, W. (2002). Directionally selective calcium signals in dendrites of starburst amacrine cells. *Nature*, *418*, 845–852.
13. Charpak, S., Mertz, J., Beaurepaire, E., Moreaux, L., & Delaney, K. (2001). Odor-evoked calcium signals in dendrites of rat mitral cells. *Proceedings of the National Academy of Sciences of the United States of America*, *98*, 1230–1234.

14. Branco, T., & Häusser, M. (2011). Synaptic integration gradients in single cortical pyramidal cell dendrites. *Neuron*, *69*, 885–892.
15. Ohki, K., Chung, S., Ch'ng, Y. H., Kara, P., & Reid, R. C. (2005). Functional imaging with cellular resolution reveals precise micro-architecture in visual cortex. *Nature*, *433*, 597–603.
16. Ohki, K., et al. (2006). Highly ordered arrangement of single neurons in orientation pinwheels. *Nature*, *442*, 925–928.
17. Hofer, S. B., et al. (2011). Differential connectivity and response dynamics of excitatory and inhibitory neurons in visual cortex. *Nature Neuroscience*, *14*, 1045–1052.
18. Ko, H., et al. (2011). Functional specificity of local synaptic connections in neocortical networks. *Nature*, *473*, 87–91.
19. Komiyama, T., et al. (2010). Learning-related fine-scale specificity imaged in motor cortex circuits of behaving mice. *Nature*, *464*, 1182–1186.
20. Petreanu, L., et al. (2012). Activity in motor-sensory projections reveals distributed coding in somatosensation. *Nature*, *489*, 299–303.
21. Orger, M. B., Kampff, A. R., Severi, K. E., Bollmann, J. H., & Engert, F. (2008). Control of visually guided behavior by distinct populations of spinal projection neurons. *Nature Neuroscience*, *11*, 327–333.
22. Nagel G, Szellas T, Huhn W, Kateriya S, Adeishvili N, Berthold P, Ollig D, Hegemann P, Bamberg E. (2003). Channelrhodopsin-2, a directly light-gated cation-selective membrane channel. *Proc Natl Acad Sci*, *100*(24), 13940–13945.
23. Boyden, E. S., Zhang, F., Bamberg, E., Nagel, G., & Deisseroth, K. (2005). Millisecond-timescale, genetically targeted optical control of neural activity. *Nature Neuroscience*, *8*, 1263–1268.
24. Zhang, F., et al. (2011). The microbial opsin family of optogenetic tools. *Cell*, *147*, 1446–1457.
25. Yizhar, O., Fenno, L. E., Davidson, T. J., Mogri, M., & Deisseroth, K. (2011). Optogenetics in neural systems. *Neuron*, *71*, 9–34.
26. Aravanis, A. M., et al. (2007). An optical neural interface: In vivo control of rodent motor cortex with integrated fiberoptic and optogenetic technology. *Journal of Neural Engineering*, *4*, 143–156.
27. Cardin, J. A., et al. (2010). Targeted optogenetic stimulation and recording of neurons in vivo using cell-type-specific expression of Channelrhodopsin-2. *Nature Protocols*, *5*, 247–254.
28. Packer, A. M., Roska, B., & Häusser, M. (2013). Targeting neurons and photons for optogenetics. *Nature Neuroscience*, *16*, 805–815.
29. Papagiakoumou, E. (2013). Optical developments for optogenetics. *Biology of the Cell/Under the Auspices of the European Cell Biology Organization*, *105*, 443–464.
30. Shepherd, G. M. G., Pologruto, T. A., & Svoboda, K. (2003). Circuit analysis of experience-dependent plasticity in the developing rat barrel cortex. *Neuron*, *38*, 277–289.
31. Shoham, S., O'Connor, D. H., Sarkisov, D. V., & Wang, S. S.-H. (2005). Rapid neurotransmitter uncaging in spatially defined patterns. *Nature Methods*, *2*, 837–843.
32. Bureau, I., von Saint Paul, F. & Svoboda, K. (2006). Interdigitated paralemniscal and lemniscal pathways in the mouse barrel cortex. *PLoS Biology*, *4*, e382.
33. Gasparini, S., & Magee, J. C. (2006). State-dependent dendritic computation in hippocampal CA1 pyramidal neurons. *The Journal of Neuroscience*, *26*, 2088–2100.
34. Branco, T., Clark, B. A., & Häusser, M. (2010). Dendritic discrimination of temporal input sequences in cortical neurons. *Science*, *329*, 1671–1675.
35. Callaway, E. M., & Katz, L. C. (1993). Photostimulation using caged glutamate reveals functional circuitry in living brain slices. *Proceedings of the National Academy of Sciences of the United States of America*, *90*, 7661–7665.
36. Wang, H., et al. (2007). High-speed mapping of synaptic connectivity using photostimulation in Channelrhodopsin-2 transgenic mice. *Proceedings of the National Academy of Sciences of the United States of America*, *104*, 8143–8148.
37. Petreanu, L., Huber, D., Sobczyk, A., & Svoboda, K. (2007). Channelrhodopsin-2-assisted circuit mapping of long-range callosal projections. *Nature Neuroscience*, *10*, 663–668.

38. Petreanu, L., Mao, T., Sternson, S. M., & Svoboda, K. (2009). The subcellular organization of neocortical excitatory connections. *Nature*, *457*, 1142–1145.
39. Glickfeld, L. L., Andermann, M. L., Bonin, V., & Reid, R. C. (2013). Cortico-cortical projections in mouse visual cortex are functionally target specific. *Nature Neuroscience*, *16*, 219–226.
40. Bonin, V., Histed, M. H., Yurgenson, S., & Reid, R. C. (2011). Local diversity and fine-scale organization of receptive fields in mouse visual cortex. *The Journal of Neuroscience*, *31*, 18506–18521.
41. Bullen, A., Patel, S. S., & Saggau, P. (1997). High-speed, random-access fluorescence microscopy: I. High-resolution optical recording with voltage-sensitive dyes and ion indicators. *Biophysical Journal*, *73*, 477–491.
42. Salomé, R., et al. (2006). Ultrafast random-access scanning in two-photon microscopy using acousto-optic deflectors. *Journal of Neuroscience Methods*, *154*, 161–174.
43. Losavio, B. E., Iyer, V., Patel, S., & Saggau, P. (2010). Acousto-optic laser scanning for multi-site photo-stimulation of single neurons in vitro. *Journal of Neural Engineering*, *7*, 045002.
44. Katona, G., et al. (2012). Fast two-photon in vivo imaging with three-dimensional random-access scanning in large tissue volumes. *Nature Methods*, *9*, 201–208.
45. Rickgauer, J. P., & Tank, D. W. (2009). Two-photon excitation of channelrhodopsin-2 at saturation. *Proceedings of the National Academy of Sciences of the United States of America*, *106*, 15025–15030.
46. Berndt, A., et al. (2011). High-efficiency channelrhodopsins for fast neuronal stimulation at low light levels. *Proceedings of the National Academy of Sciences of the United States of America*, *108*, 7595–7600.
47. Oron, D., Papagiakoumou, E., Anselmi, F., & Emiliani, V. (2012). Two-photon optogenetics. *Progress in Brain Research*, *196*, 119–143.
48. Grossman, N., et al. (2010). Multi-site optical excitation using ChR2 and micro-LED array. *Journal of Neural Engineering*, *7*, 16004.
49. Liu, J., et al. (2014). Random nanolasing in the Anderson localized regime. *Nature Nanotechnology*, *9*, 285–289.
50. James, E. L. (2011). *Fifty shades of grey*. New York: Vintage Books.
51. Bansal, V., & Saggau, P. (2013). Digital micromirror devices: Principles and applications in imaging. *Cold Spring Harbor Protocols*, *2013*, 404–411.
52. Wang, S., et al. (2007). All optical interface for parallel, remote, and spatiotemporal control of neuronal activity. *Nano letters*, *7*, 3859–3863.
53. Farah, N., Reutsky, I., & Shoham, S. (2007). Patterned optical activation of retinal ganglion cells. *Conference Proceedings Annual International Conference of the IEEE Engineering in Medicine and Biology Society*, 2007, 6368–6370.
54. Wyart, C., et al. (2009). Optogenetic dissection of a behavioural module in the vertebrate spinal cord. *Nature*, *461*, 407–410.
55. Warp, E., et al. (2012). Emergence of patterned activity in the developing zebrafish spinal cord. *Current Biology*, *22*, 93–102.
56. Guo, Z. V., Hart, A. C., & Ramanathan, S. (2009). Optical interrogation of neural circuits in *Caenorhabditis elegans*. *Nature Methods*, *6*, 891–896.
57. Leifer, A. M., Fang-Yen, C., Gershow, M., Alkema, M. J., & Samuel, A. D. T. (2011). Optogenetic manipulation of neural activity in freely moving *Caenorhabditis elegans*. *Nature Methods*, *8*, 147–152.
58. Shipley, F. B., Clark, C. M., Alkema, M. J., & Leifer, A. M. (2014). Simultaneous optogenetic manipulation and calcium imaging in freely moving *C. elegans*. *Frontiers in Neural Circuits*, *8*, 28.
59. Dhawale, A. K., Hagiwara, A., Bhalla, U. S., Murthy, V. N., & Albeanu, D. F. (2010). Non-redundant odor coding by sister mitral cells revealed by light addressable glomeruli in the mouse. *Nature Neuroscience*, *13*, 1404–1412.

60. Haddad, R., et al. (2013). Olfactory cortical neurons read out a relative time code in the olfactory bulb. *Nature Neuroscience*, *16*, 949–957.
61. Blumhagen, F., et al. (2011). Neuronal filtering of multiplexed odour representations. *Nature*, *479*, 493–498.
62. Zhu, P., Frank, T., & Friedrich, R. W. (2013). Equalization of odor representations by a network of electrically coupled inhibitory interneurons. *Nature Neuroscience*, *16*, 1678–1686.
63. Trigo, F. F., Papageorgiou, G., Corrie, J. E. T., & Ogden, D. (2009). Laser photolysis of DPNI-GABA, a tool for investigating the properties and distribution of GABA receptors and for silencing neurons in situ. *Journal of Neuroscience Methods*, *181*, 159–169.
64. Zipfel, W. R., Williams, R. M., & Webb, W. W. (2003). Nonlinear magic: Multiphoton microscopy in the biosciences. *Nature Biotechnology*, *21*, 1369–1377.
65. Helmchen, F., & Denk, W. (2005). Deep tissue two-photon microscopy. *Nature Methods*, *2*, 932–940.
66. Lutz, C., et al. (2008). Holographic photolysis of caged neurotransmitters. *Nature Methods*, *5*, 821–827.
67. Nikolenko, V., et al. (2008). SLM microscopy: Scanless two-photon imaging and photostimulation with spatial light modulators. *Frontiers in Neural Circuits*, *2*, 5.
68. Curtis, J. E., Koss, B. A., & Grier, D. G. (2002). Dynamic holographic optical tweezers. *Optics Communications*, *207*, 169–175.
69. Di Leonardo, R., Ianni, F., & Ruocco, G. (2007). Computer generation of optimal holograms for optical trap arrays. *Optics Express*, *15*, 1913–1922.
70. Spalding, G. C., Courtial, J., & Leonardo, R. Di. (Academic Press, 2008). Holographic optical tweezers. In D. L. Andrews (Ed.), *Structured Light and Its Applications*, (pp. 139–168).
71. Golan, L., Reutsky, I., Farah, N., & Shoham, S. (2009). Design and characteristics of holographic neural photo-stimulation systems. *Journal of Neural Engineering*, *6*, 066004.
72. Maschio, M. D. (2014). Novel approaches for single molecule activation and detection. 7–26. doi:10.1007/978-3-662-43367-6.
73. Botcherby, E. J., Juškaitis, R., Booth, M. J., & Wilson, T. (2008). An optical technique for remote focusing in microscopy. *Optics Communications*, *281*, 880–887.
74. Reicherter, M., Haist, T., Wagemann, E. U., & Tiziani, H. J. (1999). Optical particle trapping with computer-generated holograms written on a liquid-crystal display. *Optics Letters*, *24*, 608–610.
75. Lesem, L. B., Hirsch, P. M., & Jordan, J. A. (1969). The kinoform: A new wavefront reconstruction device. *IBM Journal of Research and Development*, *13*, 150–155.
76. Gerchberg, R. W., & Saxton, W. O. (1972). A practical algorithm for the determination of phase from image and diffraction plane pictures. *Optik*, *35*, 237–246.
77. Yang, S., et al. (2011). Three-dimensional holographic photostimulation of the dendritic arbor. *Journal of Neural Engineering*, *8*, 046002.
78. Mahajan, V. N. (2011). *Optical imaging and aberrations: Part II*. Bellingham: SPIE. doi:10.1117/3.415727.
79. Wyrowski, F., & Bryngdahl, O. (1988). Iterative Fourier-transform algorithm applied to computer holography. *Journal of the Optical Society of America A*, *5*, 1058.
80. Anselmi, F., Ventalon, C., Begue, A., Ogden, D., & Emiliani, V. (2011). Three-dimensional imaging and photostimulation by remote-focusing and holographic light patterning. *Proceedings of the National Academy of Sciences of the United States of America*, *108*, 19504–19509.
81. Papagiakoumou, E., de Sars, V., Oron, D., & Emiliani, V. (2008). Patterned two-photon illumination by spatiotemporal shaping of ultrashort pulses. *Optics Express*, *16*, 22039–22047.
82. Zahid, M., et al. (2010). Holographic photolysis for multiple cell stimulation in mouse hippocampal slices. *PLoS ONE*, *5*, e9431.
83. Papagiakoumou, E., et al. (2010). Scanless two-photon excitation of channelrhodopsin-2. *Nature Methods*, *7*, 848–854.
84. Bègue, A., et al. (2013). Two-photon excitation in scattering media by spatiotemporally shaped beams and their application in optogenetic stimulation. *Biomedical Optics Express*, *4*, 2869–2879.

85. Ambs, P., Otón, J., Millán, M. S., & Jaulin, A. (2007). Spatial light modulators for information processing: Applications and overview. *AIP Conference Proceedings* 949, 226.
86. Ronzitti, E., Guillon, M., de Sars, V., & Emiliani, V. (2012). LCoS nematic SLM characterization and modeling for diffraction efficiency optimization, zero and ghost orders suppression. *Optics Express*, 20, 17843–17855.
87. Oheim, M., Beaurepaire, E., Chaigneau, E., Mertz, J., & Charpak, S. (2001). Two-photon microscopy in brain tissue: Parameters influencing the imaging depth. *Journal of Neuroscience Methods*, 111, 29–37.
88. Beaurepaire, E., Oheim, M., & Mertz, J. (2001). Ultra-deep two-photon fluorescence excitation in turbid media. *Optics Communications*, 188, 25–29.
89. Papagiakoumou, E., et al. (2013). Functional patterned multiphoton excitation deep inside scattering tissue. *Nature Photonics*, 7, 274–278.
90. Oron, D., & Silberberg, Y. (2005). Spatiotemporal coherent control using shaped, temporally focused pulses. *Optics Express*, 13, 9903–9908.
91. Zhu, G., van Howe, J., Durst, M., Zipfel, W., & Xu, C. (2005). Simultaneous spatial and temporal focusing of femtosecond pulses. *Optics Express*, 13, 2153–2159.
92. Papagiakoumou, E., et al. (2010). Scanless two-photon excitation of channelrhodopsin-2. *Nature Methods*, 7, 848–854.
93. Packer, A. M., et al. (2012). Two-photon optogenetics of dendritic spines and neural circuits. *Nature Methods*, 9, 1202–1205.
94. Prakash, R., et al. (2012). Two-photon optogenetic toolbox for fast inhibition, excitation and bistable modulation. *Nature Methods*, 9, 1171–1179.
95. Polin, M., Ladavac, K., Lee, S.-H., Roichman, Y., & Grier, D. (2005). Optimized holographic optical traps. *Optics Express*, 13, 5831–5845.
96. Golan, L., & Shoham, S. (2009). Speckle elimination using shift-averaging in high-rate holographic projection. *Optics Express*, 17, 1330–1339.
97. Matar, S., Golan, L., & Shoham, S. (2011). Reduction of two-photon holographic speckle using shift-averaging. *Optics Express*, 19, 25891–25899.
98. Amako, J., Miura, H., & Sonehara, T. (1995). Speckle-noise reduction on kinoform reconstruction using a phase-only spatial light modulator. *Applied Optics*, 34, 3165–3171.
99. Jesacher A. (2008). Advanced shaping of light fields with cascaded spatial light modulators. PhD Thesis. Innsbruck Medical University.
100. Glückstad, J. (1996). Phase contrast image synthesis. *Optics Communications*, 130, 225–230.
101. Papagiakoumou, E., et al. (2010). Scanless two-photon excitation of channelrhodopsin-2. *Nature Methods*, 7, 848–854. doi:10.1038/nmeth.1505.
102. Theer, P., Hasan, M. T., & Denk, W. (2003). Two-photon imaging to a depth of 1000 microm in living brains by use of a Ti:Al₂O₃ regenerative amplifier. *Optics Letters*, 28, 1022–1024.
103. Dal Maschio, M., et al. (2010). Simultaneous two-photon imaging and photo-stimulation with structured light illumination. *Optics Express*, 18, 18720–18731.
104. Emiliani, V., et al. (2005). Wave front engineering for microscopy of living cells. *Optics Express*, 13, 1395–1405.
105. Dal Maschio, M., De Stasi, A. M., Benfenati, F., & Fellin, T. (2011). Three-dimensional in vivo scanning microscopy with inertia-free focus control. *Optics Letters*, 36, 3503–3505.
106. Quirin, S., Jackson, J., Peterka, D. S., & Yuste, R. (2014). Simultaneous imaging of neural activity in three dimensions. *Frontiers in Neural Circuits*, 8, 29.
107. Botcherby, E. J., et al. (2012). Aberration-free three-dimensional multiphoton imaging of neuronal activity at kHz rates. *Proceedings of the National Academy of Sciences of the United States of America*, 109, 2919–2924.
108. Kner, P., Sedat, J. W., Agard, D. A., & Kam, Z. (2010). High-resolution wide-field microscopy with adaptive optics for spherical aberration correction and motionless focusing. *Journal of Microscopy*, 237, 136–147.

109. Grewe, B. F., Voigt, F. F., van 't Hoff, M., & Helmchen, F. (2011). Fast two-layer two-photon imaging of neuronal cell populations using an electrically tunable lens. *Biomedical Optics Express*, *2*, 2035–2046.
110. Fahrbach, F. O., Voigt, F. F., Schmid, B., Helmchen, F., & Huisken, J. (2013). Rapid 3D light-sheet microscopy with a tunable lens. *Optics Express*, *21*, 21010–21026.
111. Kirkby, P. A., Srinivas Nadella, K. M. N., & Silver, R. A. (2010). A compact Acousto-Optic Lens for 2D and 3D femtosecond based 2-photon microscopy. *Optics Express*, *18*, 13721–13745.
112. Dufresne, E. R., Spalding, G. C., Dearing, M. T., Sheets, S. A., & Grier, D. G. (2000). Computer-generated holographic optical tweezer arrays. *Review of Scientific Instruments*, *72*, 1810–1816.
113. Reutsky-Gefen, I., et al. (2013). Holographic optogenetic stimulation of patterned neuronal activity for vision restoration. *Nature Communications*, *4*, 1509.
114. Yang, S., et al. (2011). Three-dimensional holographic photostimulation of the dendritic arbor. *Journal of Neural Engineering*, *8*, 046002.
115. Yang, S., Emiliani, V., & Tang, C.-M. (2014). The kinetics of multibranch integration on the dendritic arbor of CA1 pyramidal neurons. *Frontiers in Cellular Neuroscience*, *8*, 127.
116. Watson, B. O., et al. (2010). Two-photon microscopy with diffractive optical elements and spatial light modulators. *Frontiers in Neuroscience*, *4*, 1–8.
117. Ducros, M., Goulam Houssen, Y., Bradley, J., de Sars, V., & Charpak, S. (2013). Encoded multisite two-photon microscopy. *Proceedings of the National Academy of Sciences of the United States of America*, *110*, 13138–13143.